Catalysis Today 158 (2010) 401–408

Contents lists available at ScienceDirect

Catalysis Today

journal homepage: www.elsevier.com/locate/cattod

Core–shell structured nanoparticles ($M@SiO_2$, Al_2O_3, MgO; M = Fe, Co, Ni, Ru) and their application in CO_x-free H_2 production via NH_3 decomposition

L.H. Yao[a,b], Y.X. Li[a,b], J. Zhao[b], W.J. Ji[b,*], C.T. Au[a,**]

[a] Department of Chemistry, Center for Surface Analysis and Research, Hong Kong Baptist University, Kowloon Tong, Hong Kong, China
[b] The Key Laboratory of Mesoscopic Chemistry, Ministry of Education, School of Chemistry and Chemical Engineering, Nanjing University, Nanjing 210093, China

ARTICLE INFO

Article history:
Available online 11 June 2010

Keywords:
Core–shell structure
Nanoparticles
Hydrogen
Ammonia decomposition

ABSTRACT

The core–shell nanostructures ($M@SiO_2$, Al_2O_3, MgO; M = Fe, Co, Ni, Ru) are synthesized and applied in the production of CO_x-free H_2 through NH_3 decomposition. The characterization results indicate that the dimension and dispersion of the core particles is dependent on the core constitution, and the shell encapsulation effect (thickness of shell, single or hierarchical enwrapping) is determined by the nature of cores as well as the core–shell interaction. The core property can also be influenced by core starting material and nominal core/shell ratio. The obtained core–shell catalysts show not only superior activity but also better stability than the naked nanoparticles or the supported counterparts. The presence of stable shells provides the unique environment around cores, functioning as microcapsular-like reactors in which adsorption and catalytic reaction are enhanced on the cores. The stable shells effectively prevent the core particles from aggregation during reaction.

1. Introduction

The on-site generation of hydrogen is essential for proton-exchange membrane fuel cells (PEMFCs) [1–4]. The hydrogen production directly from carbonaceous compounds such as methanol and methane has its limitations because the CO_x side products degrade the cell performance even at extremely low concentrations [5–9]. Alternatively, the direct generation of CO_x-free hydrogen through catalytic ammonia decomposition has been considered [2,3,5–21]. Many kinds of catalytic materials have been studied for this purpose [7,11,14–16,21–25]. Ru and Ni are found to be the most active among the noble and cheap metals, respectively. Among various supported metal catalysts, the carbon nanotubes (CNTs)-supported Ru catalysts are outstanding in terms of catalytic activity [16,22–25].

Core–shell structured materials have attracted great attentions in recent years because of the unique structural feature and physicochemical properties [26–28]. Silica encapsulated nanoparticles (NPs) have been studied in the fields of biology, optics, electronics, magnetism, and sensing [8,9,29]. Enwrapping a nano-material in a stable shell can enhance the stability and compatibility of the core material and in addition, cause a change in electron charge, reactivity and functionality of the enwrapped material [30,31].

The application of NPs in heterogeneous catalysis is highly desirable due to the intrinsic "surface effects". Unfortunately, NPs are unstable and aggregate easily at elevated temperatures. The aim of the present study is to investigate the feasibility of retaining the intrinsic character of NPs by having them encapsulated inside a porous but stable shell. Our previous study revealed that encapsulation of the Fe NPs with a porous silica shell can not only considerably enhance catalyst activity but also significantly improve its stability [32]. In the present study, we prepared the core–shell structures with different core and shell constitutions and made a systematic comparison on their physicochemical properties and catalytic behaviors. It has been revealed that the characteristics and catalytic activity of the core–shell catalysts are strongly dependent upon the constitution of core and shell as well as the specific core–shell interaction.

2. Experimental

2.1. Catalyst preparation

2.1.1. Preparation of metal oxide core NPs

Fe_2O_3 NPs: Typically, 4.04 g of $Fe(NO_3)_3{\cdot}6H_2O$ (Sigma–Aldrich, 0.01 mol) was added to 100 ml of distilled water containing 3.00 g of polyethylene glycol (PEG-20000, Fluka). After the solution was stirred for 30 min, 4.5 g of urea was added and the mixture was heated to 80 °C and kept at this temperature for 6 h. The precipitate

* Corresponding author. Tel.: +86 25 83686270; fax: +86 25 83317761.
** Corresponding author. Fax: +852 34117348.
E-mail addresses: jiwj@nju.edu.cn, jiwjnju@yahoo.com (W.J. Ji), pctau@hkbu.edu.hk (C.T. Au).

0920-5861/$ – see front matter © 2010 Elsevier B.V. All rights reserved.
doi:10.1016/j.cattod.2010.05.009

Table 1
Surface areas of the representative core–shell structures before reduction.

Catalyst	Nano-Fe_2O_3@SiO_2 (Si/Fe = 0.2)	Nano-NiO@SiO_2 (Si/Ni = 0.2)	Nano-RuO_2@SiO_2 (Si/Ru = 0.2)	Nano-Fe_2O_3@Al_2O_3 (Al/Fe = 0.2)
S.A. (m^2/g)	34	112	42	38

was collected by centrifugation, washed with ethanol and distilled water, dried at 100 °C for 10 h, and calcined in air at 500 °C for 4 h.

NiO NPs: Typically, 2.9 g of $Ni(NO_3)_2{\cdot}6H_2O$ (Sigma–Aldrich, 0.01 mol) was added to 100 ml of distilled water containing 3.0 g of polyethylene glycol (PEG-20000, Fluka). After the solution was stirred for 30 min, 4.5 g of urea was added and the mixture was heated to 85 °C and kept at this temperature for 24 h. The precipitate was collected by centrifugation, washed with ethanol and distilled water, dried at 100 °C for 10 h, and calcined in air at 400 °C for 4 h.

RuO_2 NPs: Typically, 2.1 g of $RuCl_3$ (Sigma–Aldrich, 0.01 mol) was added to 300 ml of distilled water containing 6.0 g of cyltrimethylammonium bromide (CTAB, ACROS). After 30 min of stirring, the pH of the solution was adjusted to 9 by the slow addition of aqueous ammonia. The mixture was then heated to 60 °C and kept at this temperature for 12 h. The solid product was collected by centrifugation, washed with ethanol and distilled water, dried at 100 °C for 12 h, and calcined in air at 550 °C for 4 h.

2.1.2. Preparation of Fe, Ni, Co and Ru NPs encapsulated by SiO_2, Al_2O_3 or MgO

Certain amount of oxide core NPs (for example, 0.67 g RuO_2 NPs) was added to 50 ml of anhydrous ethanol and subjected to a 30-min supersonic treatment. Then 10 ml of $NH_3{\cdot}H_2O$ and a designated amount of TEOS (depending on the specific Si/M (M = Fe, Ni, Co, Ru) ratio) was added under sonication (1 h) in an ultrasound bath (KQ-100DE, 40 kHz, 100 W). The product was collected by drying at 80–100 °C for 10 h and subject to in situ reduction in a 25% H_2/Ar flow at 550 °C for 2 h. The as-obtained catalysts are denoted as nano-M@SiO_2 (M = Fe, Ni, Co, Ru) hereinafter. The encapsulation of oxide cores by Al_2O_3 or MgO shell is similarly performed using aluminum isoproxide or magnesium nitrate as the raw material.

2.2. Characterization

The specific surface area of the samples was measured on a NOVA1200 apparatus. XRD analysis was performed on a Philips X'Pert MPD Pro X-ray diffractometer with graphite monochromatized Cu Kα radiation (λ = 0.1541 nm). TEM images were taken on a JEM-1010 TEM microscope. High Resolution TEM (HRTEM) images were recorded on a FEI Tecnai G2 20S-twin transmission electron microscope. Hydrogen temperature-programmed desorption (H_2-TPD) was carried out to estimate the surface exposure of metallic cores: 100 mg of sample was pretreated in a flow of 25% H_2/Ar at 550 °C for 2 h. After cooled to RT, the sample was purged with pure He at RT for 0.5 h, and then heated to 600 °C at a rate of 10 °C/min.

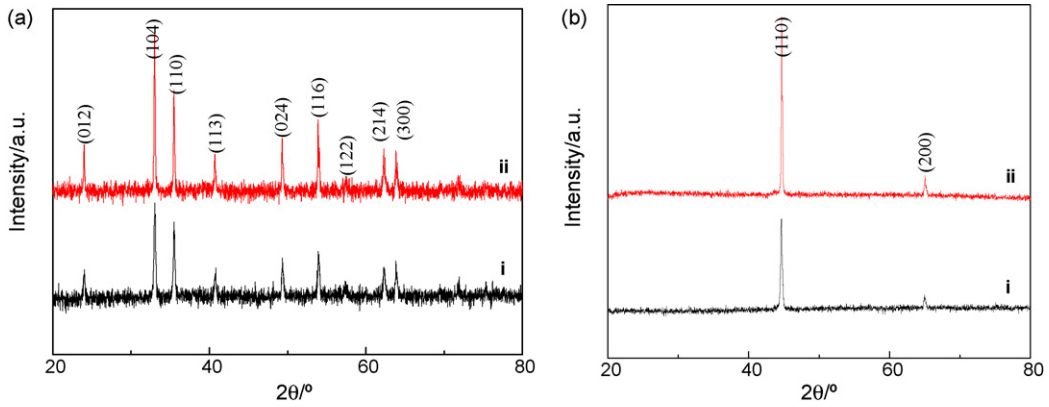

Fig. 1. XRD patterns of (a) nano-Fe_2O_3@SiO_2 (Si/Fe = 0.2) and (b) nano-Fe@SiO_2 (Si/Fe = 0.2) core–shell structures prepared with different starting ferric salts (samples i and ii are prepared with $Fe(NO_3)_3$ and $FeCl_3$, respectively).

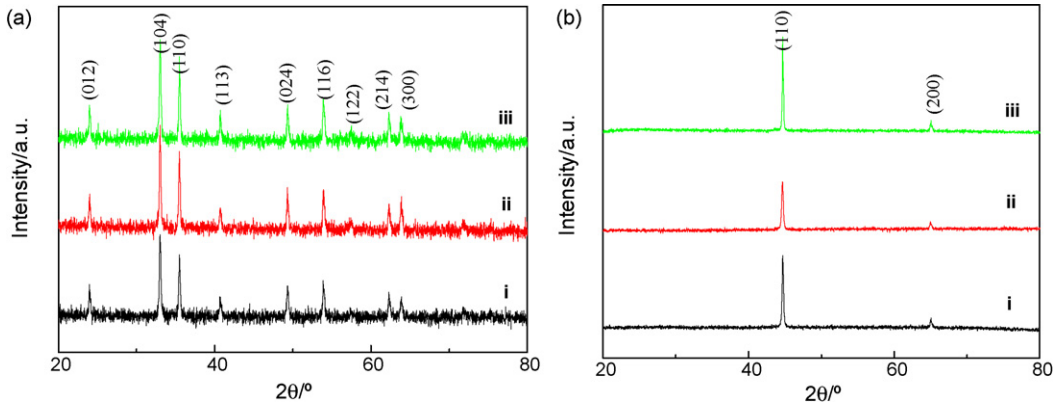

Fig. 2. XRD patterns of (a) nano-Fe_2O_3@SiO_2 and (b) nano-Fe@SiO_2 core–shell structures prepared with different nominal Si/Fe atomic ratios (samples i, ii, and iii are prepared with the Si/Fe ratio of 0.1, 0.2, and 0.4, respectively).

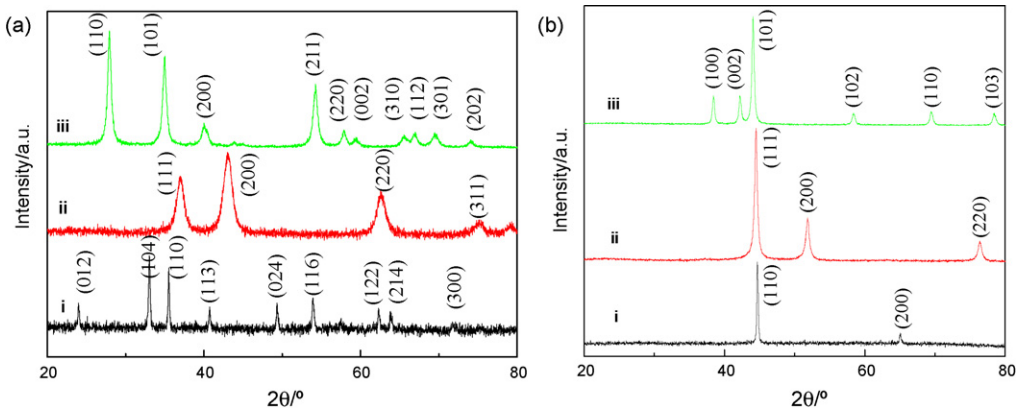

Fig. 3. XRD patterns of (a) the nano-Fe_2O_3@SiO_2 (i), nano-NiO@SiO_2 (ii), and nano-RuO_2@SiO_2 (iii); and (b) the nano-Fe@SiO_2 (i), nano-Ni@SiO_2 (ii), and nano-Ru@SiO_2 (iii). Si/M = 0.2, M = Fe, Ni, Ru.

2.3. Catalytic activity

Catalytic activity was evaluated in a continuous-flow quartz reactor (catalyst: 100 mg, 60–80 mesh) under pure NH_3 (flow rate = 50 ml/min) in the temperature range of 400–700 °C. Before reaction, the catalyst was reduced in situ in a 25% H_2/Ar flow at 550 °C for 2 h, then purged with a flow of pure Ar. The activity data at a certain temperature was collected after the reaction became stable. Product analysis was performed on an on-line gas chromatograph (Shimadzu or GC122) equipped with thermo-conductive detector and Poropak Q column, using He as a carrier gas. NH_3 conversion in a blank reactor was <1.0% at 550 °C.

3. Results and discussion

3.1. Catalyst characterization

3.1.1. BET surface area

Shown in Table 1 are the BET surface areas of the nano-Fe_2O_3@SiO_2, nano-NiO@SiO_2, nano-Ru_2O_3@SiO_2 and nano-Fe_2O_3@Al_2O_3. Except for the nano-NiO@SiO_2, the other three samples show similar surface areas (34–42 m^2/g). The nano-NiO@SiO_2 has much large surface area (112 m^2/g). Note that the measured surface area is determined by the nature of cores as well as the character of shells. Therefore, the large surface area of nano-

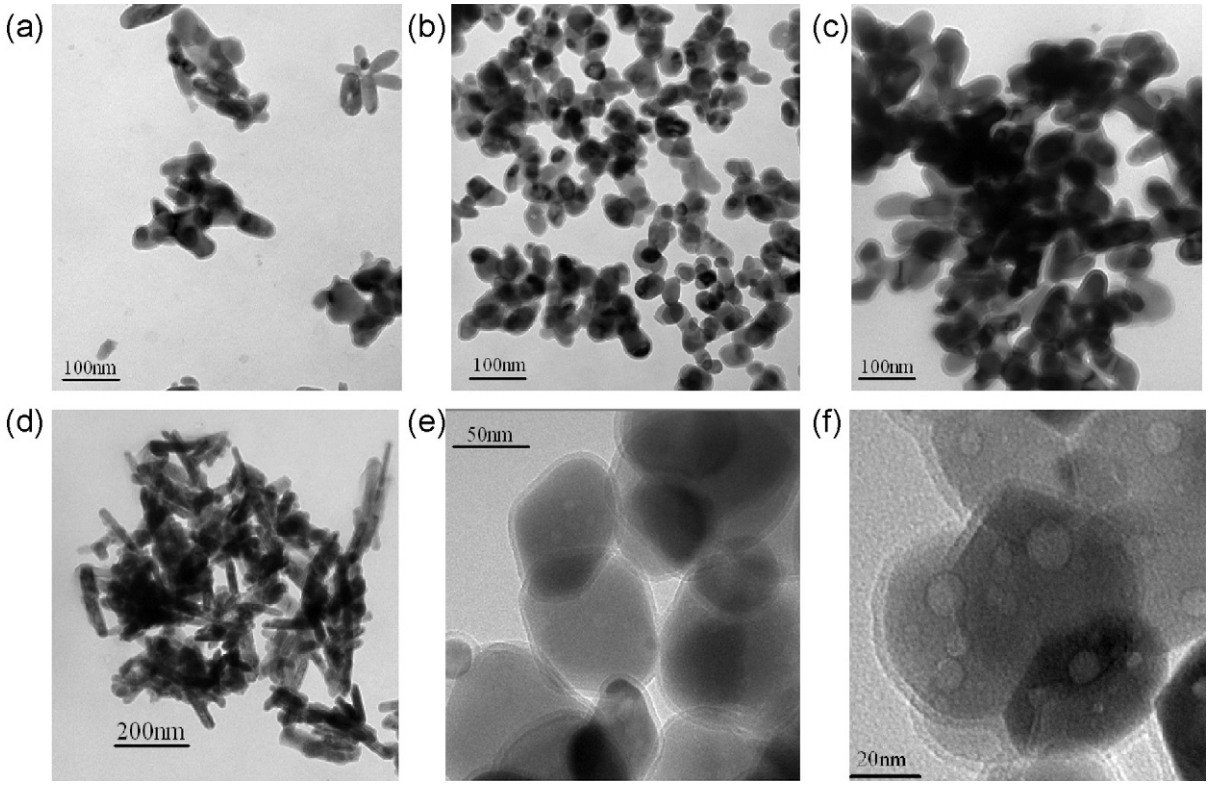

Fig. 4. TEM images of: (a–c) the nano-Fe_2O_3@SiO_2 prepared using the Si/Fe ratio of 0.1, 0.2, and 0.4, respectively; (d) the nanorod-Fe_2O_3@SiO_2 (Si/Fe = 0.2); (e) HRTEM image of sample b; and (f) HRTEM image of nano-Fe_2O_3@Al_2O_3 (Al/Fe = 0.2).

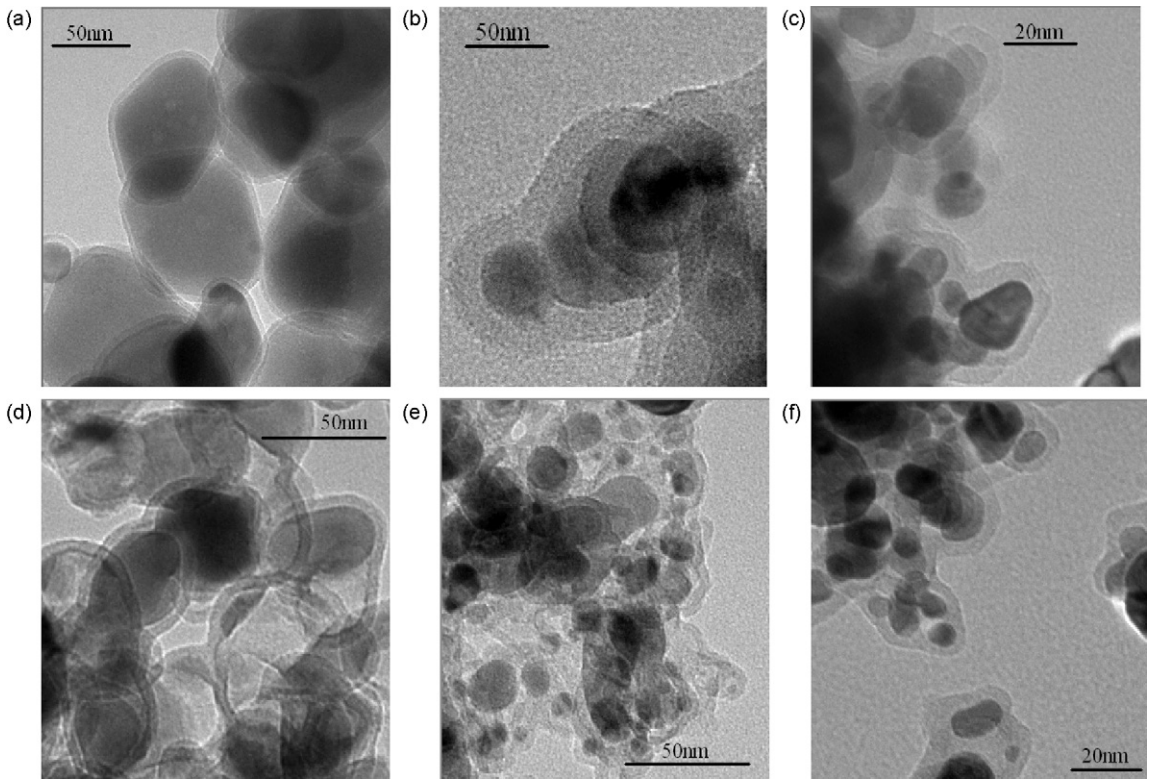

Fig. 5. HRTEM images of: (a–c) nano-Fe_2O_3@SiO_2, nano-NiO@SiO_2, and nano-RuO_2@SiO_2, respectively; (d–f) nano-Fe@SiO_2, nano-Ni@SiO_2, and nano-Ru@SiO_2, respectively. Si/M = 0.2, M = Fe, Ni, Ru.

NiO@SiO_2 is likely due to the shell character such as the thicker SiO_2 shell. This deduction is confirmed by the TEM observation (see below).

3.1.2. XRD

Fig. 1 shows the XRD patterns of the nano-Fe_2O_3@SiO_2 and nano-Fe@SiO_2 prepared with different starting ferric salts. It is revealed that when $FeCl_3$ is used as the starting material for preparation, relatively higher crystallinity of nano-Fe_2O_3 and nano-Fe cores can be achieved.

The XRD results of the nano-Fe_2O_3@SiO_2 and nano-Fe@SiO_2 prepared using different Si/Fe ratios are shown in Fig. 2. The nominal Si/Fe ratio does not show a notable influence on the nano-Fe_2O_3 cores (Fig. 3a), but it may have an impact on the character of nano-Fe cores (Fig. 2b): difference in crystallinity of nano-Fe cores can be observed due to adopting different Si/Fe ratios. Such difference could be a result of nano-Fe_2O_3 core reduction which can be affected by the thickness of silica shells and the contact between the nano-Fe_2O_3 cores and SiO_2 shells. The XRD results (not shown) also revealed that there is little effect of $Fe(NO_3)_3$ concentration (0.033, 0.066, and 0.132 mol/l, respectively) on the nano-Fe_2O_3 cores. In all cases, Fe_2O_3 cores are completely transformed into metallic Fe when subject to an in situ reduction in 25% H_2/Ar mixture at 550 °C for 2 h.

Shown in Fig. 3a are the XRD patterns of nano-Fe_2O_3@SiO_2, nano-NiO@SiO_2, and nano-RuO_2@SiO_2. There are only α-e_2O_3, NiO, and RuO_2 phases can be identified. After being subject to the in situ reduction at 550 °C for 2 h in 25% H_2/Ar mixture, the diffraction peaks of core components can be indexed to the metallic Fe, Ni, and Ru, respectively (Fig. 3b). The results suggest that the Fe_2O_3, NiO, and RuO_2 cores are entirely reduced to the corresponding metallic form under the adopted in situ reduction conditions.

3.1.3. TEM

The morphology of various core–shell structures before and after H_2-reduction has been investigated and the results are shown in Figs. 4 and 5. Fig. 4a–c shows the TEM images of the nano-Fe_2O_3@SiO_2 prepared using different Si/Fe ratios. It appears that the Si/Fe ratio shows an effect on the aggregation of Fe_2O_3 NPs as well as the thickness of SiO_2 shells. The thickness of SiO_2 shells increases with increasing Si/Fe ratio in preparation. At a Si/Fe ratio = 0.2, there are more uniformly dispersed Fe_2O_3 NPs (Fig. 4b). Fig. 4d shows the TEM image of the Fe_2O_3 nanorods encapsulated by SiO_2 shells. The dimension of the Fe_2O_3 nanorod core is approximately 150–200 nm in length and ca. 50 nm in diameter. The TEM image

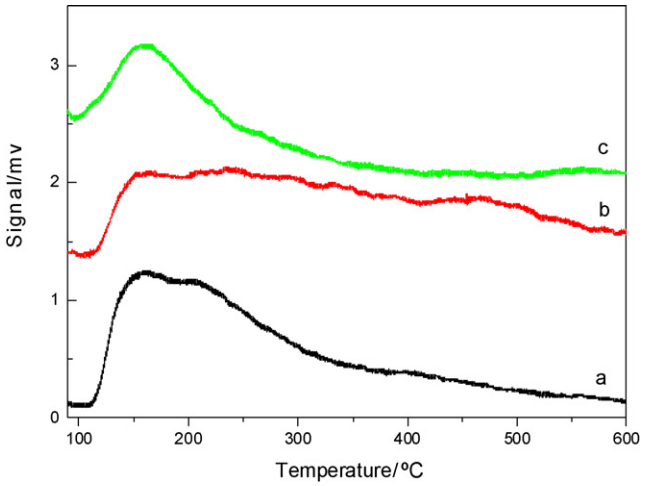

Fig. 6. H_2-TPD profiles of (a) Fe@SiO_2 (Si/Fe = 0.2), (b) Ni@SiO_2 (Si/Ni = 0.2), (c) Ru@SiO_2 (Si/Ru = 0.2).

Table 2
Surface metal exposure of the representative core–shell catalysts.

Catalyst	Nano-Fe@SiO_2 (Si/Fe = 0.2)	Nano-Ni@SiO_2 (Si/Ni = 0.2)	Nano-Ru@SiO_2 (Si/Ru = 0.2)
Surface metal exposure ($\mu mol/g_{cat}$)	31.7	30.1	27.7

of nano-Fe_2O_3@SiO_2 (Si/Fe = 0.2) at higher magnification (Fig. 4e) indicates the Fe_2O_3 cores of 50–100 nm in size are completely encapsulated by a thin uniform SiO_2 shells (5–8 nm). The HRTEM image of the nano-Fe_2O_3@Al_2O_3 (Si/Fe = 0.2) (Fig. 4f) indicates the uniform encapsulation of Fe_2O_3 NPs by a thin layer of Al_2O_3 (~5 nm in thickness).

Shown in Fig. 5a–c are the HRTEM images of nano-Fe_2O_3@SiO_2, nano-NiO@SiO_2, and nano-RuO_2@SiO_2. It can be clearly observed that the morphology of core–shell structures is highly dependent upon the nature of core components: not only the size and dispersion of cores but also the thickness and encapsulation of shells can be largely different. In the case of nano-RuO_2@SiO_2, the size of RuO_2 core is comparatively small (10–20 nm), but the aggregation of RuO_2 cores is obvious, and there is the formation of hierarchical SiO_2 shells. The HRTEM images (Fig. 5a–c) indicate different thickness of SiO_2 shells for nano-Fe_2O_3@SiO_2, nano-NiO@SiO_2, and nano-RuO_2@SiO_2, and in the case of nano-NiO@SiO_2, the SiO_2 shells are found to be the thickest. Our previous investigation [32] revealed that the specific surface area of naked nano-Fe_2O_3 particles is ca. 18 m^2/g, while that of nano-Fe_2O_3 particles encapsulated by SiO_2 shell around 35 m^2/g, which demonstrates the SiO_2 coating is porous and has a contribution to the total surface area of the core–shell catalyst. Therefore, the larger specific surface area of nano-NiO@SiO_2 is mainly due to the contribution of thicker SiO_2 shell. Shown in Fig. 5d–f are the HRTEM images of nano-Fe@SiO_2, nano-Ni@SiO_2, and nano-Ru@SiO_2, respectively. The hierarchical SiO_2 shell encapsulation is more obvious in the case of nano-Ru@SiO_2.

In the catalyst precursors, the cores are in the oxide form and the shell layers and core particles are closely contacted. In the activated catalysts which are subject to in situ reduction, the core oxides are completely transformed into metallic particles. Owing to the removal of lattice oxygen of the core, there is core shrinkage and hence the space between the core and shell, resulting in "microcapsular-like" structures which are clearly evidenced in Fig. 5d–f. Such a unique environment around the cores can function as microcapsular-like reactor [33–36] in which the reactant molecules are enriched (confinement effect). Similar phenomenon has been reported recently over the carbon nanotubes encapsulated Fe nanoparticles [37].

3.1.4. H_2-TPD

Fig. 6 illustrates the H_2-TPD profiles of the core–shell nano-Fe@SiO_2, nano-Ni@SiO_2, and nano-Ru@SiO_2 catalysts. The H_2-desorption over nano-Fe@SiO_2 and nano-Ru@SiO_2 appears similar, the desorption peak temperatures are 20–30 °C lower than that over K-Ru/MCM-41 and K-Ni/MCM-41 [17]. Note that the H_2-desorption peak over nano-Ni@SiO_2 becomes board, implying a non-uniformity of adsorption sites. Apparently, the nano-Fe@SiO_2 shows the largest H_2-desorption peak, indicating that there are more exposed surface Fe atoms.

Based on the peak area of the H_2-TPD profiles and a standard calibration of CuO reduction, the H_2-chemisorption uptake and the surface metal exposure can be estimated (Table 2, assuming adsorption of one H atom per metal atom [10]). It was revealed that the nano-Fe@SiO_2 has the largest surface metal exposure while the nano-Ru@SiO_2 the smallest. Similar tendency was also observed over the K-Ni/MCM-41 and K-Ru/MCM-41 catalysts [17]. This observation may also in part account for the difference in their catalytic behaviors shown below.

3.2. Catalytic performance

3.2.1. Nano-Fe@SiO_2

Shown in Fig. 7a are the catalytic activities of the nano-Fe@SiO_2 samples prepared using different concentrations of $Fe(NO_3)_3$ solution. Similar catalyst behavior can be observed over the three samples, and this is not surprising because nearly identical core–shell structures are obtained in the form of either nano-Fe_2O_3@SiO_2 before H_2-reduction or nano-Fe@SiO_2 after reduction. Fig. 7b demonstrates the catalytic activity of the nano-Fe@SiO_2 samples prepared using different Fe-starting materials. It is observed that using $Fe(NO_3)_3$ as the starting material can result in notably more active core–shell catalyst. According to the XRD results (Fig. 1b), the crystallinity of the Fe cores obtained with $Fe(NO_3)_3$ is comparatively low, therefore, there could be more defects existing in these Fe cores and functioning as the highly active sites for the reaction. Fig. 7c shows the catalytic behaviors of the nano-Fe@SiO_2 samples prepared using different Si/Fe ratios. There seems an optimal Si/Fe ratio to generate the core–shell structure which is more active than the other two catalysts. In terms of the XRD and TEM characterizations, small size and uniform dispersion of the core–shell structure and low structural regularity of the Fe NPs may account for the enhanced catalytic performance.

3.2.2. Naked Fe NPs, nano-Fe, Ni@SiO_2, Al_2O_3, MgO

Fig. 8a presents the temperature dependence of NH_3 conversion over the Fe@SiO_2 nanorods and Fe@SiO_2 NPs. There is a large difference observed in catalyst performance. Such a big deviation in catalyst activity strongly implies that the core morphology and reaction environment (the space between the core outer surface and the internal shell wall) are vital for reaction proceeding. Fig. 8b shows the catalyst activity over the naked Fe NPs and the core–shell Fe@SiO_2 and Fe@Al_2O_3 catalysts at elevated temperatures. The core–shell nanostructures perform notably better than the naked Fe NPs. The results suggest the core–shell structure may provide a unique core environment beneficial for the reaction. It is also observed that the nano-Fe@Al_2O_3 performs better than the nano-Fe@SiO_2 especially at low temperatures. In comparison of nano-Fe@Al_2O_3 with nano-Fe@SiO_2, the constitution as well as particle size of core is the same, while the constitution of shell is different (Al_2O_3 vs. SiO_2). In view of the TEM images shown in Fig. 4e and f, one can find the thickness of Al_2O_3 and SiO_2 shells is comparable. However, the interaction between the Fe core and the Al_2O_3 and SiO_2 shells (similar to metal-support interaction) can be different, which in turn can modify the nature of Fe core. Moreover, the texture and porosity of Al_2O_3 and SiO_2 shells may also be different, which could have an impact on the mass transportation and consequently catalytic activity. The comparison of NH_3 conversions over the nano-Ni@SiO_2, nano-Ni@MgO and nano-Ni@Al_2O_3 is made in Fig. 8c. For the same Ni cores, SiO_2 shell presents the best performance as compared with MgO and Al_2O_3 shells. Based on the results of Fig. 8b and c, one can conclude that not only the core element but also the shell constitution as well as the involved core–shell interaction determine the catalytic behavior of core–shell structures.

3.2.3. Nano-Fe, Co, Ni, Ru@SiO_2

Shown in Fig. 9 is the comparison of NH_3 conversions over the core–shell M@SiO_2 (M = Fe, Co, Ni, Ru) catalysts in the temperature range of 400–700 °C. Among these core–shell structures, the nano-Ru@SiO_2 performs significantly better than the other three

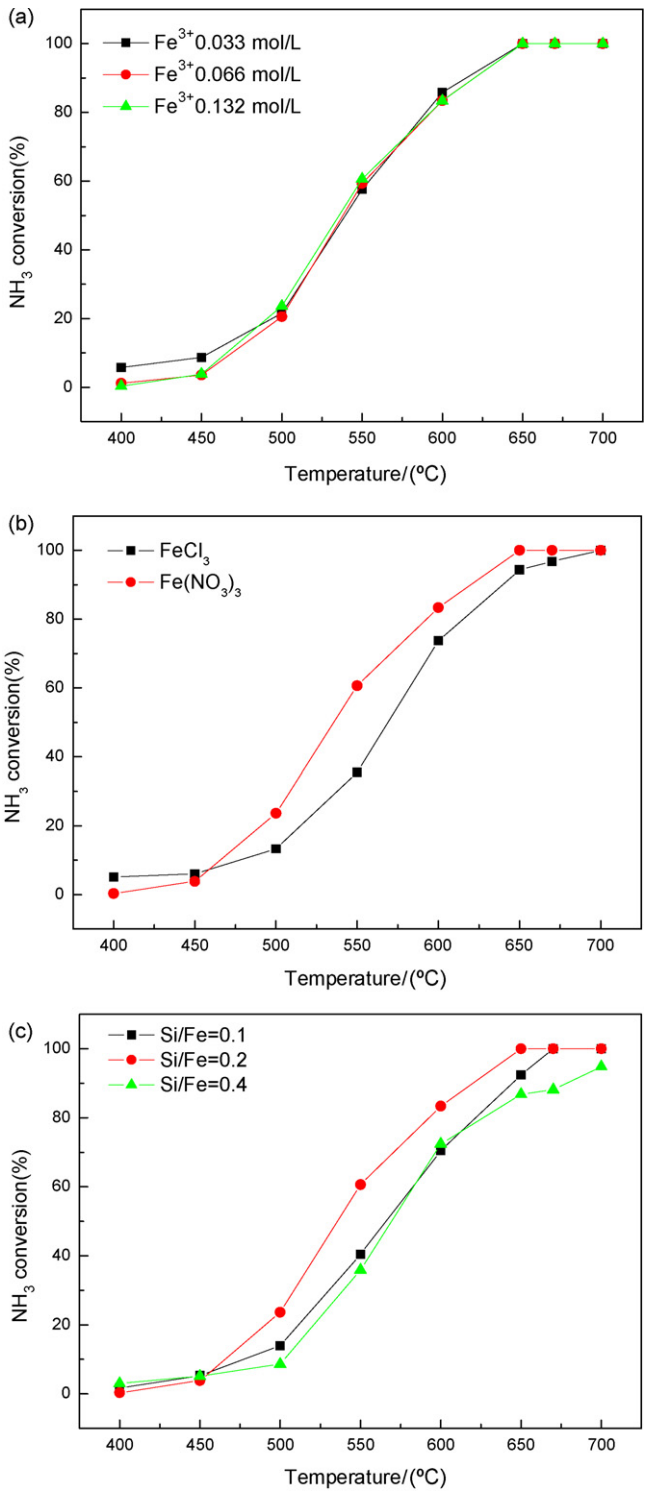

Fig. 7. Temperature dependence of NH_3 conversion over various core–shell $Fe@SiO_2$ catalysts. (a) Prepared with different concentration of $Fe(NO_3)_3$ solution; (b) prepared with different starting ferric salts; and (c) prepared with different nominal Si/Fe atomic ratios.

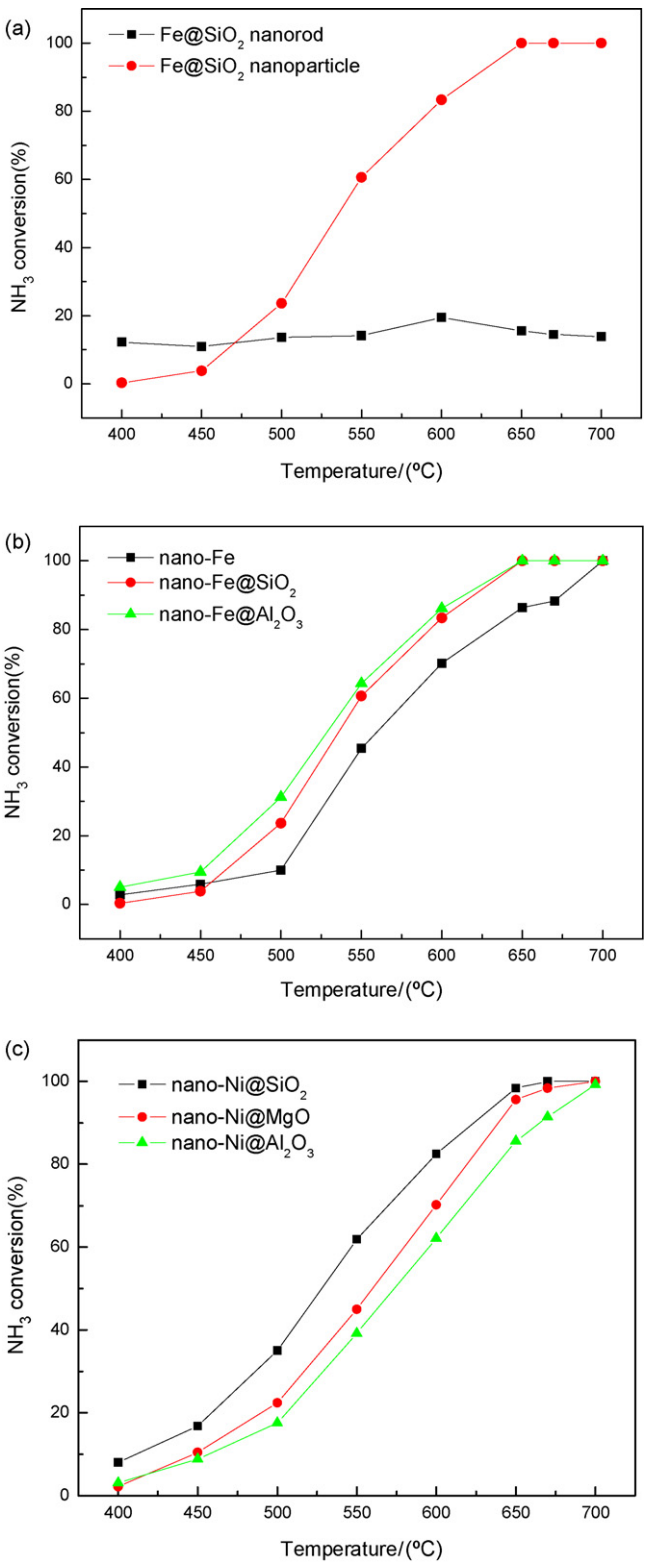

Fig. 8. NH_3 conversion at elevated temperatures over various core–shell structured catalysts. (a) $Fe@SiO_2$ nanorods and NPs; (b) Fe NPs, nano-$Fe@SiO_2$, and nano-$Fe@Al_2O_3$; and (c) nano-$Ni@SiO_2$, nano-Ni@MgO, and nano-Ni@ Al_2O_3.

catalysts: 100% NH_3 conversion can be obtained at a temperature as low as 550 °C. This is the most active catalyst known to date for the target reaction. Among the core–shell structures containing VIII metals, the nano-$Fe@SiO_2$ is slightly more active than the nano-$Ni@SiO_2$ beyond 550 °C, but both are superior to the nano-$Co@SiO_2$. The results suggested that the catalyst activity of core–shell structure is strongly dependent on the nature of core element. Actually the chemical nature of cores has an effect on the size, morphology and dispersion of the cores, the thickness and encapsulation of shells (Fig. 5), and the core–shell interaction.

Table 3 presents the H_2 formation rates in the typical temperature range of 500–670 °C over the nano-$Fe@SiO_2$, nano-$Ni@SiO_2$,

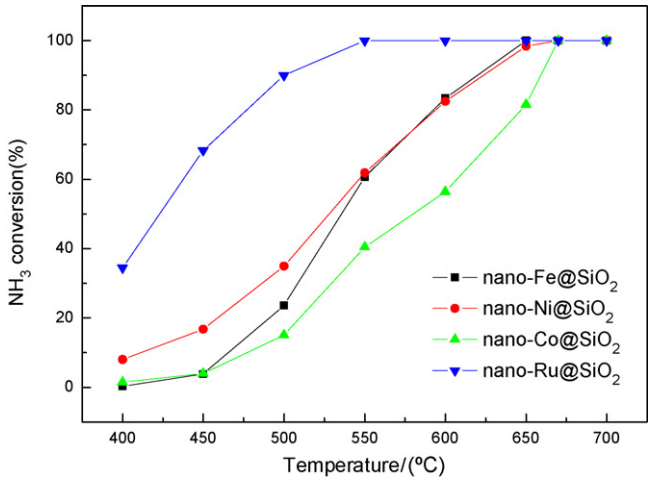

Fig. 9. Temperature dependence of NH_3 conversion over nano-Fe@SiO_2, nano-Ni@SiO_2, nano-Co@SiO_2, and nano-Ru@ SiO_2.

and nano-Ru@SiO_2. The nano-Ru@SiO_2 catalyst is extremely active and the most efficient for H_2 production among the three kinds of core–shell catalysts. On the other hand, although the nano-Ni@SiO_2 is more active than the nano-Fe@SiO_2 in the 500–550 °C range, the latter performs better at temperatures beyond 600 °C.

Based on the temperature dependence of NH_3 conversion (Fig. 9) and the H_2 formation rates at various temperatures (Table 3), one can observe that the core–shell structured catalysts are more active than the SiO_2 [10] and MCM-41 [17] supported ones. It is emphasized that one should make the comparison with caution among these catalysts because the metal loadings as well as dispersions are different across the catalysts. The size of cores (in core–shell catalysts) is similar to that of the naked metal NPs but larger than that of metal particles supported on SiO_2 [10] and MCM-41 [17], therefore, on the basis of per unit mass of catalyst, there are declines in exposure of surface metal atoms in the core–shell catalysts. Nevertheless, the core–shell structures can provide a unique environment around the cores and function as microcapsular-like reactors [33–36] in which the space between the cores and internal shell surfaces is enriched with reactant molecules. Such confinement effect of reactant molecules occurs inside the hollow shells and is similar to that reported inside the carbon nanotubes [37], resulting in enhanced adsorption and catalytic reaction on the core surfaces. In other words, despite there is a decline in exposure of surface metal atoms (per unit mass of catalyst), the core–shell catalysts are catalytically more active than the naked metal NPs or conventional supported ones. Our latest results obtained over the core–shell structured Ru@SiO_2 with filled or partially filled cores (of comparable size) reveal that the core–shell Ru@SiO_2 with partially filled Ru cores does exhibit superior activity. On the other hand, due to the difference in thickness and constitution of shells, mass transportation could somehow vary over the core–shell catalysts, in part accounting for difference of reactions. It is revealed that the difference in catalytic activity observed over the naked NPs, the supported ones and the core–shell structures are mainly due to the variation in

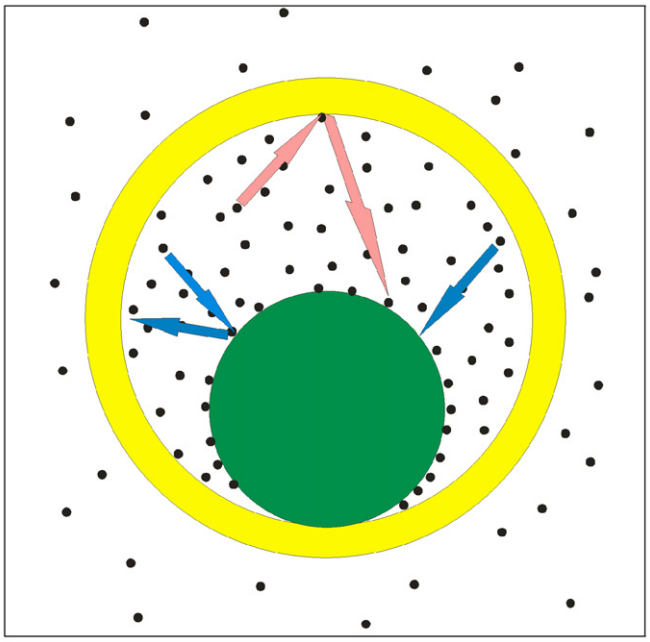

Scheme 1. The illustration of enhanced adsorption and reaction in the microcapsular-like reactor of core–shell catalyst.

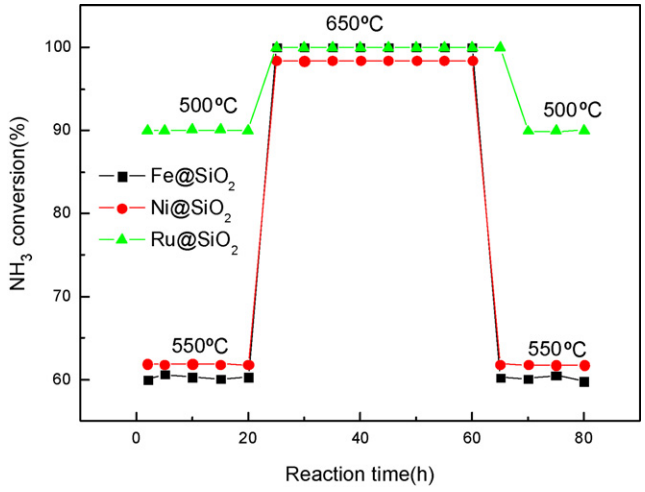

Fig. 10. Stability test of the nano-Fe@SiO_2, nano-Ni@SiO_2, and nano-Ru@SiO_2 catalysts.

catalyst structures and particularly in local reaction environment (Scheme 1).

3.3. Catalyst stability

Fig. 10 shows the stability of the three core–shell catalysts under the selected reaction conditions. All the catalysts were tested at an ammonia conversion within the range of 60–90%. For the nano-

Table 3
H_2 Formation rate (mmol/min g_{cat}) over the core–shell catalysts.

Temperature (°C)	Fe@SiO_2 (Si/Fe = 0.2)	Ni@SiO_2 (Si/Ni = 0.2)	Ru@SiO_2 (Si/Ru = 0.2)	K-Ni/MCM-41(TIE) [17]	10%Ni/SiO_2 [10]
500	7.9	11.7	30.1	10.7	3.3
550	20.3	20.7	33.5	17.3	6.8
600	27.9	27.6	33.5	24.5	11.4
650	33.5	33.0	33.5	31.1	21.1
670	33.5	33.5	33.5	32.5	–

Fe@SiO_2 and nano-Ni@SiO_2, ammonia conversion is ca. 60% at 550 °C, while for the nano-Ru@SiO_2, ammonia conversion is ca. 90% at 500 °C. All the three catalysts retain their activities after a cycle of temperature raising (after 20 h at 500 or 550 °C) to 650 °C, maintaining at 650 °C for 40 h (giving ~100% ammonia conversion), and lowering to 500 or 550 °C. The results indicate that the core–shell structured catalysts are stable at these conditions.

4. Concluding remarks

In the present study, the core–shell nanostructures (M@SiO_2, Al_2O_3, MgO; M = Fe, Co, Ni, Ru) were synthesized as the novel catalysts for the production of CO_x-free H_2 through NH_3 decomposition. It was found that the core property is closely related to the core constitution and its starting material as well as the nominal core/shell ratio, while the shell encapsulation effect (thickness of shell, single or hierarchical enwrapping) is dependent upon the core nature as well as the core–shell interaction. The obtained core–shell catalysts show superior activity and stability to the naked NPs or the supported counterparts. The core–shell structured NPs can provide the unique environment around cores and function as microcapsular-like reactors in which the reactant molecules can be enriched. The consequence is enhanced adsorption and catalytic reaction on the cores. Such effect is significant for the core–shell structured catalysts (Scheme 1); this is because although the measured surface metal exposure of cores per unit mass of catalyst is lower than that of the conventional supported metal particles, the core–shell catalysts are more active than the supported catalysts. Furthermore, the core–shell catalysts also show better stability than the naked or supported NPs owing to the stable shells that effectively prevent the core NPs from aggregation during reaction [32].

Acknowledgements

We acknowledge the financial support of the RGC, HKSAR (RGC 200107) and the invitation of the APCSEET2009 organizing committee to give a keynote presentation.

References

[1] R.Z. Sorensen, L.J.E. Nielsen, S. Jensen, O. Hansen, T. Johannessen, U. Quaade, C.H. Christensen, Catal. Commun. 6 (2005) 229–232.
[2] S.F. Yin, B.Q. Xu, X.P. Zhou, C.T. Au, Appl. Catal. A 277 (2004) 1–9.
[3] R. Metkemeijer, P. Achard, J. Power Sources 49 (1994) 271–282.
[4] W. Arabczyk, J. Zamlynny, Catal. Lett. 60 (1999) 167–171.
[5] J. Hepola, P. Simell, Appl. Catal. B 14 (1997) 287–303.
[6] P.A. Simell, J.O. Hepola, A.O. Krause, Fuel 76 (1997) 1117–1127.
[7] G. Papapolymerou, V. Bontozoglou, J. Mol. Catal. A: Chem. 120 (1997) 165–171.
[8] P. Reiss, J. Bleuse, A. Pron, Nano Lett. 2 (2002) 781–784.
[9] V. Skumryev, S. Stoyanov, Y. Zhang, G. Hadjipanayis, D. Givord, J. Nogues, Nature 423 (2003) 850–853.
[10] T.V. Choudhary, C. Svadinaragana, D.W. Goodman, Catal. Lett. 72 (2001) 197–201.
[11] W. Rarog, Z. Kowalczyk, J. Sentek, D. Skladanowski, D. Szmigiel, J. Zielinski, Appl. Catal. A 208 (2001) 213–216.
[12] W. Raróg, D. Szmigiel, Z. Kowalczyk, S. Jodzis, J. Zielinski, J. Catal. 218 (2003) 465–469.
[13] A. Jedynak, Z. Kowalczyk, D. Szmigiel, W. Raróg, J. Zielinski, Appl. Catal. A 237 (2002) 223–226.
[14] D.A. Goetsch, S.J. Schmit, WO Patent 0 187 770 (2001).
[15] M.E.E. Abashar, Y.S. Al-Sughair, I.S. Al-Mutaz, Appl. Catal. A 236 (2002) 35–53.
[16] S.F. Yin, Q.H. Zhang, B.Q. Xu, W.X. Zhu, C.F. Ng, C.T. Au, J. Catal. 224 (2004) 384–396.
[17] X.K. Li, W.J. Ji, J. Zhao, S.J. Wang, C.T. Au, J. Catal. 236 (2005) 181–189.
[18] J.G. Choi, J. Catal. 182 (1999) 104–116.
[19] K. Hashimoto, N. Toukai, J. Mol. Catal. A: Chem. 161 (2000) 171–178.
[20] M.C.J. Bradford, P.E. Fanning, M.A. Vannice, J. Catal. 172 (1997) 479–484.
[21] H. Dietrich, K. Jacobi, G. Ert, Surf. Sci. 352 (1996) 138–141.
[22] S.F. Yin, B.Q. Xu, C.F. Ng, C.T. Au, Appl. Catal. B: Environ. 48 (2004) 237–241.
[23] S.F. Yin, B.Q. Xu, S.J. Wang, C.F. Ng, C.T. Au, Catal. Lett. 96 (2004) 113–116.
[24] S.F. Yin, B.Q. Xu, W.X. Zhu, C.F. Ng, X.P. Zhou, C.T. Au, Catal. Today 93 (2004) 27–38.
[25] S.J. Wang, S.F. Yin, L. Li, B.Q. Xu, C.F. Ng, C.T. Au, Appl. Catal. B: Environ. 52 (2004) 287–299.
[26] Y.H. Deng, W.L. Yang, C.H. Wang, S.K. Fu, Adv. Mater. 15 (2003) 1729–1732.
[27] J. Yang, J.Y. Lee, H.-P. Too, J. Phys. Chem. B 109 (2005) 19208–19212.
[28] M.A. Malik, P. O'Brien, N. Revaprasadu, Chem. Mater. 14 (2002) 2004–2010.
[29] Y.H. Deng, D.W. Qi, C.H. Deng, X.M. Zhang, D.Y. Zhao, J. Am. Chem. Soc. 130 (2008) 28–29.
[30] K.P. Velikov, A. Moroz, A. van Blaaderen, Appl. Phys. Lett. 80 (2002) 49–51.
[31] F. Grasset, N. Labhsetwar, D. Li, D.C. Park, N. Saito, H. Haneda, O. Cador, T. Roisnel, S. Mornet, E. Duguet, J. Portier, J. Etourneau, Langmuir 18 (2002) 8209–8216.
[32] Y.X. Li, S.Q. Liu, L.H. Yao, W.J. Ji, C.T. Au, Catal. Commun. 11 (2010) 368–372.
[33] J. Wu, F.P. Hu, X.D. Hu, Z.D. Wei, P.K. Shen, Electrochim. Acta 53 (2008) 8341–8345.
[34] W.M. Zhang, J.S. Hu, Y.G. Guo, S.F. Zheng, L.S. Zhong, W.G. Song, L.J. Wan, Adv. Mater. 20 (2008) 1160–1165.
[35] S.H. Joo, P.J. Young, C.K. Tsung, Y. Yamada, P.D. Yang, G.A. Somorjai, Nat. Mater. 8 (2009) 126–131.
[36] J. Shi, N. Ren, Y.H. Zhang, Y. Tang, Prog. Chem. 21 (2009) 1750–1756.
[37] X.L. Pan, X.H. Bao, Chem. Commun. (2008) 6271–6281.